Journal of
Materials Chemistry A

PAPER

View Article Online
View Journal

Cite this: DOI: 10.1039/d6ta03298b

Temperature-controlled anti-solvent engineering enables the fabrication of reproducible and stable tin-based perovskite solar cells by decoupling the kinetic fragility

Tingting Liu,[a] Ryosuke Nishikubo,*[ab] Chien-Yu Chen,[c] Atsushi Wakamiya[c] and Akinori Saeki*[ab]

Received 20th April 2026
Accepted 27th May 2026

DOI: 10.1039/d6ta03298b

rsc.li/materials-a

Tin-based perovskites are among the most promising lead-free, solution-processed photovoltaic absorbers. However, their practical deployment is limited by uncontrolled crystallization kinetics, a narrow process window and severe energetic disorder resulting from rapid nucleation. Here, we demonstrate that modulation of anti-solvent temperature (cool to hot anti-solvent treatment) leads to a significant impact on crystallinity, grain packing and electronic features of the films. This transformation allows for governing the crystallization process with temperature and makes it fabrication-tolerant. We also examine the pre-annealing passivation of precursor films (passivation before post-thermal annealing). This dual control suppresses energetic disorder and non-radiative recombination without altering the optical bandgap or absorbance. This improvement increases the power conversion efficiency from 3.50% to 9.12%. *In situ* optical spectroscopy reveals a dramatic change in perovskite formation during the post-annealing process. Our synergistic control of thermal processes enhances efficiency, operational stability and reproducibility, paving the way to overcome defects in tin-halide perovskite photovoltaics.

Introduction

The development of lead-free perovskite solar cells (PSCs) is urgent for sustainable and environmentally acceptable light energy harvest. Among the emerging candidates,[1–7] tin (Sn)-based perovskites[8–11] are widely regarded as the most promising alternatives to lead counterparts[12–15] owing to their suitable bandgap,[16,17] high carrier mobility and applicability to low-temperature solution processing. Despite rapid advances in power conversion efficiency (PCE), Sn-based PSCs still lag behind their Pb-based counterparts in both efficiency and operational reliability. While state-of-the-art Pb-based PSCs have achieved certified PCEs exceeding 26%,[15] Sn-based PSCs continue to suffer from poor reproducibility due to their narrow fabrication window and kinetically dominated crystallization process. These challenges have impeded both mechanistic understanding and scalable manufacturing.[18–24]

The chemically active $5s^2$ lone pair of Sn^{2+} endows tin halide perovskites with higher Lewis acidity compared with their lead counterparts, resulting in intensified coordination dynamics, rapid crystallization and heightened oxidation vulnerability.[25–27] Such intrinsic fragility renders Sn–PSCs highly sensitive to processing perturbations, frequently leading to morphological integrity and defect-rich multicrystalline films. Extensive efforts have been devoted to addressing these issues through additive engineering,[28–38] surface passivation[39–41] and compositional tuning.[42–50] While such approaches can partially suppress uncontrolled crystal growth and reduce defect density, they often impose additional structural complexity. Consequently, direct stabilization of the nucleation process remains comparatively unexplored. Establishing control over the earliest stages of intermediate formation may offer a reliable route to suppressed disorder and an expanded fabrication window.

Recent studies have demonstrated that interfacial passivation plays a critical role in suppressing defect-assisted non-radiative recombination and improving the operational stability of Sn-based perovskite solar cells. Various strategies, including using organic ammonium salts,[2,51–53] multifunctional ligands,[54,55] and fluorinated molecules[56,57] have been developed to regulate surface energetics, suppress Sn^{2+} oxidation, and reduce trap-state density. In particular, fluorinated chemicals[58–60] have attracted increasing attention owing to their strong electron-withdrawing characteristics and favourable

---

[a] Department of Applied Chemistry, Graduate School of Engineering, The University of Osaka, 2-1 Yamadaoka, Suita, Osaka 565-0871, Japan. E-mail: nishikubo@chem.eng.osaka-u.ac.jp; saeki@chem.eng.osaka-u.ac.jp

[b] Innovative Catalysis Science Division, Institute for Open and Transdisciplinary Research Initiatives (ICS-OTRI), The University of Osaka, 1-1 Yamadaoka, Suita, Osaka 565-0871, Japan

[c] Institute for Chemical Research, Kyoto University, Gokasho, Uji, Kyoto 611-0011, Japan

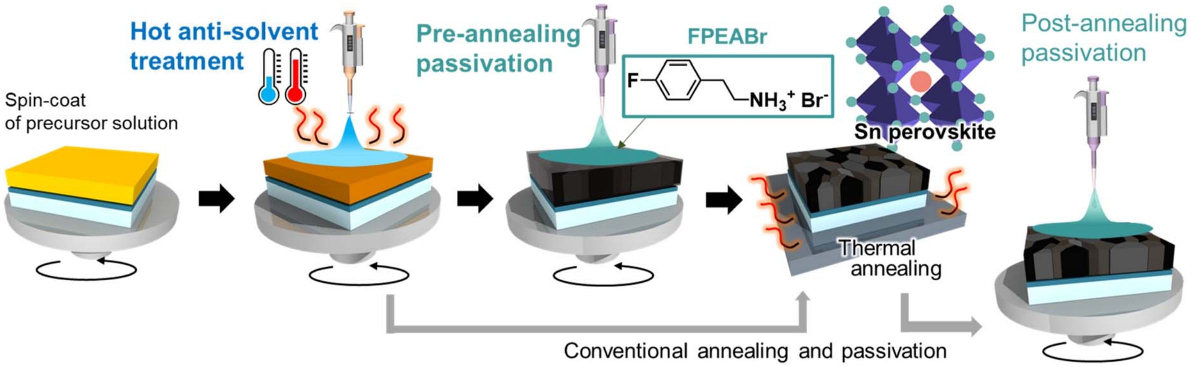

Fig. 1 Schematic of hot anti-solvent treatment and pre-annealing passivation to decouple the kinetic fragility and transfer to temperature-controlled nucleation and growth (the black arrows). The process represented by the grey arrows is conventional post-annealing passivation.

interactions with the Sn–I framework, which can effectively improve lattice stability and carrier dynamics. Despite these advances, most reported passivation strategies are applied after film crystallization, where their effects are mainly limited to surface defect modification. Therefore, understanding how passivation molecules influence crystallization pathways and intermediate-phase evolution during film formation remains an important challenge for further improving the efficiency and reproducibility of Sn-based perovskite solar cells.

Here we introduce thermal engineering of anti-solvent that decouples the stabilization of nucleation from the growth of Sn-based perovskite multi-grains (Fig. 1). Compared with conventional additive engineering or multi-step surface passivation approaches, thermal engineering offers several practical advantages, including process simplicity, compatibility with existing spin-coating protocols, and minimal modification to precursor chemistry. More importantly, temperature regulation can be readily integrated into scalable fabrication methods without introducing excessive compositional complexity or additional purification requirements. Accordingly, by controlling the anti-solvent temperature (13–135 °C), we demonstrate the formation of spatially homogeneous intermediate phases during the nucleation stage, which alters the crystallization process from a kinetically fragile process into a temperature-governed regime. *In situ* UV-vis photoabsorption (PA) and photoluminescence (PL) monitoring[61] reveal accelerated PL evolution, accompanied by enlarged grain size, reduced energetic disorder, and markedly broadened processing tolerance. Building upon this stabilized nucleation framework, the sequential thermal annealing and pre-annealing passivation (passivation before annealing) are further examined to enable controlled growth of multigrain films. These two sequential yet synergistic processes not only enhance PCEs and operational stability but also improve reproducibility of Sn–PSCs.

Results and discussion

Control of anti-solvent temperature to define the nucleation regime

To elucidate how anti-solvent temperature governs the crystallization pathway of Sn-based perovskites, the temperature of anti-solvent toluene was changed from 13 to 135 °C and applied to spin-coating of $PEA_{0.1}FA_{0.9}Sn\ I_3$ (PEA: phenylethylammonium and FA: formamidinium) on a poly(3,4-ethylenedioxythiophene) polystyrene sulfonate (PEDOT:PSS) hole transport material. All of the films after spin-coating were post-annealed on a hot plate at 80 °C for 20 min. As shown in the scanning electron microscope (SEM) images in Fig. 2a (13, 65, 105, and 125 °C) and Fig. S1 (SI) (13–125 °C by 5–10 °C step), pronounced morphological evolution due to the anti-solvent temperature was observed. At the low temperatures (<45 °C), the films exhibited discontinuous grains, rough surfaces, and pin holes, indicative of sluggish solvent extraction and spatially heterogeneous nucleation. Increasing the anti-solvent temperature (55–95 °C) markedly improved film uniformity, producing compact and well-fused grains. Our results are consistent with the previous report on hot anti-solvent treatment (HAT) of Sn-based 3D perovskites that show an optimal anti-solvent temperature of 65 °C.[35] A rapid homogenization of host solvent and poor hot anti-solvent is suggested to enable efficient mixing, spontaneous supersaturation, and uniform nucleation. In our observation, a distinct structural merit emerges at a high temperature of 105 °C, where densely packed grains with minimal intergranular voids are obtained. When the temperature exceeds 115 °C, crystallization becomes excessively abrupt, limiting grain coarsening despite full surface coverage.

X-ray diffraction (XRD) further reveals temperature-activated crystallization (Fig. 2b). While the low-temperature films (<65 °C) are dominated by the diffraction peaks of (100) at $2\theta = 14.0°$ and (200) at $2\theta = 28.2°$, those of (210) at $2\theta = 31.6°$ and (220) at $2\theta = 40°$ emerge above 55–75 °C and intensify toward 125 °C, indicating a subtle change in crystallite orientation. Simultaneously the crystallite size calculated using Scherrer's equation at the (100) peak (L_{100}) shows a gradual decreasing trend with the temperature.

As observed in the macroscopic appearance of the films in the still images in Fig. 3a, the 105 °C film exhibits a darker and more uniform surface than the 65 °C film, suggesting improved structural continuity and reduced optical scattering. These macroscopic (optical images) and microscopic (SEM images) observations suggest better multicrystalline morphology of high-temperature quenched films than low-temperature ones,

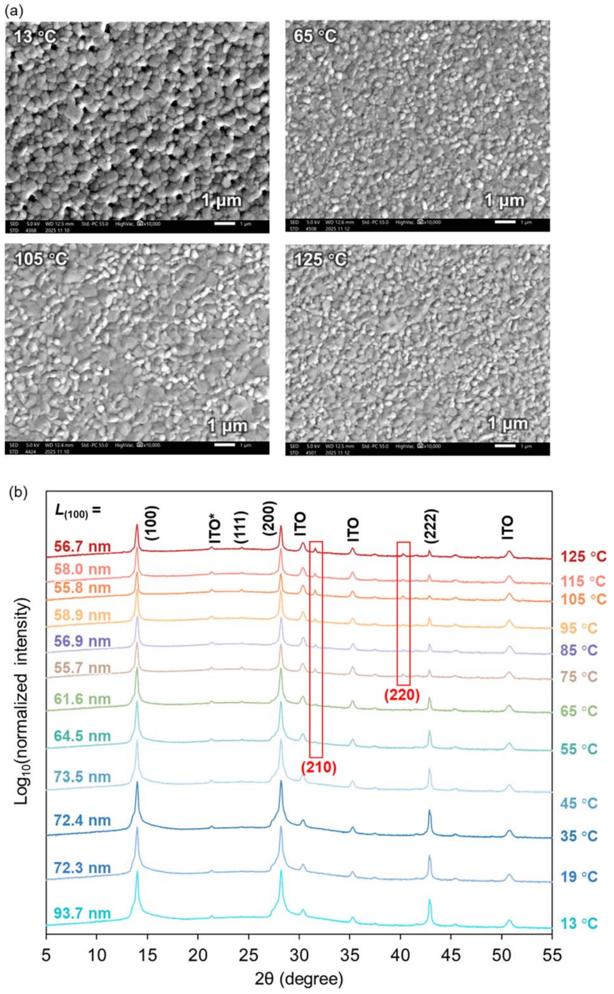

Fig. 2 Temperature-dependent microstructure evolution of $PEA_{0.1}FA_{0.9}SnI_3$ films at different anti-solvent temperatures. (a) Top-view SEM images (the scale bar: 1 μm) and (b) XRD patterns. The crystallite size (L_{100}) calculated using Scherrer's equation at the (100) peak is appended. The peak intensity at ITO* was used for the intensity normalization.

although the crystallinity of the former is decreased. PA spectroscopy reveals systematic band-edge evolution with increasing anti-solvent temperature (Fig. 3b and S2a–b (SI)). With the increase in the anti-solvent temperature, peak-like features in the 500–600 nm region progressively disappear and accompany a slight widening of the optical bandgap (E_g) from 1.41 to 1.44 eV. The higher absorbance at low temperature is attributed to increased film thickness and enhanced light scattering within the film (Fig. S3 (SI)). This enlarged E_g is likely associated with suppressed band-tail states and reduced structural disorder at elevated anti-solvent temperatures. Correspondingly, the Urbach energy (E_U) obtained from the band edge decreases monotonically from 53.3 meV (13 °C) to 45.8 meV (65 °C) and further to 34.9 meV (105 °C), indicating substantial reduction of band tail states and energetic disorder (Fig. 3c and S2c–d (SI)).

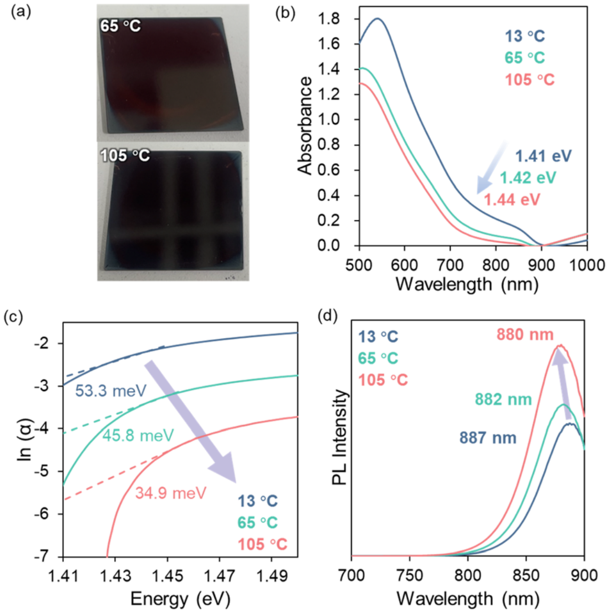

Fig. 3 Temperature-dependent photophysical properties of $PEA_{0.1}FA_{0.9}SnI_3$ films at different anti-solvent temperatures. (a) Visual comparison of as-fabricated films prepared by hot anti-solvent at 65 and 105 °C. (b) Photoabsorption spectra (E_g appended), (c) Urbach energy (E_U appended) extracted from ln(α) plots (α: absorption coefficient in arbitrary units), and (d) PL spectra (the peak wavelength appended) of the films quenched at different anti-solvent temperatures (13, 65 and 105 °C) followed by 80 °C one-step post-annealing for 20 min.

Steady-state PL measurements corroborate this trend (Fig. 3d and S4 (SI)). The PL intensity increases progressively with temperature, while the emission peak shifts from 887 nm (13 °C) to 882 nm (65 °C) and 880 nm (105 °C) in line with the widening of E_g. The enhanced emission indicates suppressed non-radiative recombination, consistent with reduced E_U. Films processed by post-annealing at three-step sequential temperatures (45–65–100 °C for 10 min for each)[35] follow an identical trend (Note S1 (SI), Fig. S5–S8 (SI)) with the 1-step post-annealing at 80 °C in terms of PL intensities and SEM morphologies. These results confirm that the electronic and morphological properties are predominantly governed by the anti-solvent temperature rather than the post-annealing process.

Interestingly, the 105 °C-quenched film exhibits more pronounced stability than the 65 °C-quenched film in ambient air (18.7 °C and relative humidity = 30%) as shown in Fig. S9 (SI). While the 65 °C-quenched film quickly lightens and develops spatial inhomogeneity, the 105 °C-quenched film retains a homogeneous appearance with markedly suppressed degradation over time (>60 min). The distinct temporal evolution highlights the improved environmental robustness imparted by the high-temperature quenching regime.

The difference in optimal HAT temperature between this work and previous study[35] would originate from the distinct crystallization kinetics of the precursor systems. In

$MA_{0.25}FA_{0.75}SnI_3$ (MA: methylammonium), the presence of the small and more dynamic MA^+ cations likely leads to relatively fast crystallization, where a moderate anti-solvent temperature (65 °C) is sufficient to achieve controlled nucleation and film formation. In contrast, in our $PEA_{0.1}FA_{0.9}SnI_3$, the bulky PEA^+ cation introduces steric hindrance and retards crystallization, requiring a higher anti-solvent temperature (105 °C) to promote nucleation and grain growth. Therefore, the higher temperature (more thermal energy) is presumably required in the PEA/FA system to slow crystallization kinetics and achieve improved film quality and device performance.

Device characterization with hot anti-solvent and varied process parameters

Device performance was compared between the 65 °C and the optimized 105 °C anti-solvent temperatures (Fig. 4a). A significant enhancement in photovoltaic output was achieved at 105 °C, with the champion PCE increasing from 3.50% to 6.31%. This improvement originates from concurrent gains in short-circuit current density (J_{sc}) from 19.20 to 21.17 mA cm^{-2}, open-circuit voltage (V_{oc}) from 0.363 to 0.427 V, and fill factor (FF) from 0.516 to 0.706 (Tables S1–S2 (SI)), consistent with the photophysical and SEM results. Integrated current densities derived from the external quantum efficiency (EQE) spectra agree well with the J_{sc} values (Fig. 4b), confirming metric reliability. Importantly, the enhanced EQE is not solely governed by optical absorption but is predominantly attributed to improved carrier collection efficiency arising from reduced E_U (Fig. 3c) and suppressed non-radiative recombination (Fig. 3d). Notably, a trend of temperature-defined crystallization remains preserved in alternative post-annealing protocols (1 step or 3 step), although the optimal anti-solvent window shifts accordingly (Note S1 (SI), Fig. S10–S12 (SI) and Tables S1–S2 (SI)).

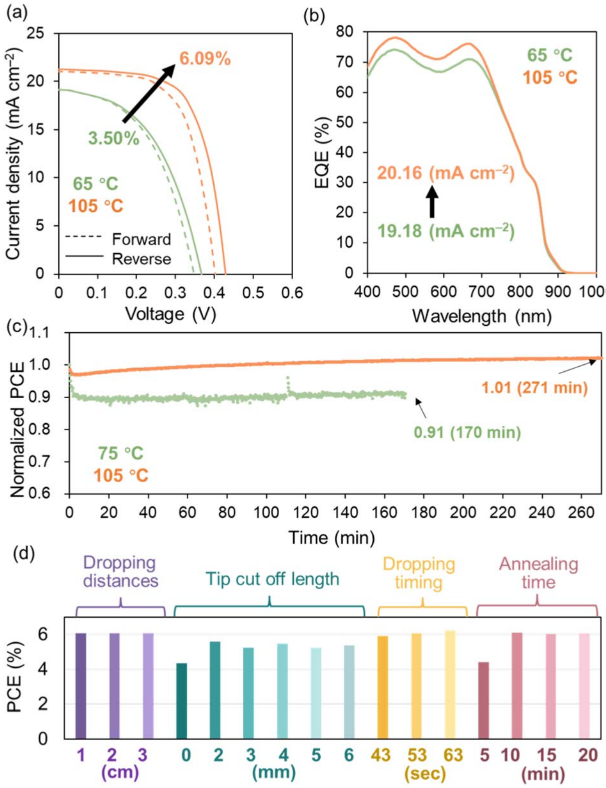

Fig. 4 Device performance of $PEA_{0.1}FA_{0.9}SnI_3$ solar cells fabricated using various anti-solvent temperatures (65 and 105 °C). (a) Representative *J*–*V* curves (maximum PCE appended), (b) EQE spectra (integrated J_{SC} appended), and (c) normalized time-dependent PCEs of 75 and 105 °C-quenched devices. Solid and dotted lines correspond to forward and reverse *J*–*V* scans, respectively. A 75 °C-quenched device rather than a 65 °C-quenched device was used for the stability measurements, because the latter was extremely unstable. The initial PCEs are as shown in Table S3. (d) Summary of PCE responses to four anti-solvent processing parameters (dropping distance, tip cut off length, dropping timing, and post-annealing time) based on 145 devices, indicating minimal sensitivity and a wide process window.

Furthermore, operational stability was simultaneously enhanced. Under continuous 1-sun illumination, the 105 °C-quenched device retains normalized performance at 1.02 after 272 min (4.5 h), whereas that of the 75 °C-quenched device decreases to 0.91 after 170 min (2.8 h) (Fig. 4c). Devices fabricated at intermediate temperatures exhibit consistent trends (Fig. S13 (SI) and Table S3 (SI)). These results using a high-temperature anti-solvent connect the improvement of initial PCE with its operational lifetime.

To evaluate fabrication robustness, key processing parameters—including anti-solvent dropping distance (0.3–3 cm), cut off length of a 1 mL pipette-tip (0–6 mm corresponding to the hole with a 1.0–3.5 mm diameter), anti-solvent volume (160–560 μL), dropping timing (13–63 s), and annealing duration (5–20 min)—were systematically examined at the 105 °C anti-solvent temperature (Note S2 (SI), Fig. S14–S31 (SI) and Tables S4–S7 (SI)). Remarkably, substantial variations in all five parameters result in minor changes in morphology, XRD crystallinity, photophysical properties, and maximum PCE (Fig. 4d) as long as some parameters are within the certain regions (dropping distance >1 cm, tip cut off length >2 mm (corresponding to opening diameters >1.5 mm) and annealing duration >10 min). This insensitivity indicates that high-temperature anti-solvent shifts nucleation from a turbulence-sensitive kinetic regime to a temperature-governed intermediate-mediated pathway, thereby broadening the processing window and improving reproducibility.

Exploration of passivation molecules and annealing management

Although the 105 °C anti-solvent treatment significantly improved the intermediate-phase quality and device performance compared to the 65 °C condition, the PCE was still below the expectations, requiring further optimization of film formation and defect management. Based on the SEM and PL characterization studies, we systematically explored multiple strategies including pre-heating of a substrate (Fig. S32 (SI)), reduction in the amount of Sn powder (Fig. S33 (SI)), size of the anti-solvent pipette tip (Fig. S34 (SI)), aging of precursor solution (Fig. S35 (SI)), additives in precursor solutions (MASCN, NH_4SCN, $Pb(SCN)_2$, and $Sn(SCN)_2$, Fig. S36–S37 (SI)), additives

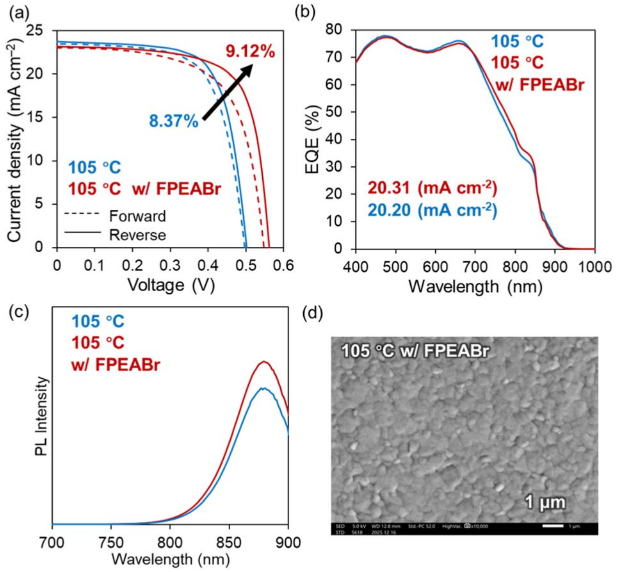

Fig. 5 Device performance of optimized $PEA_{0.1}FA_{0.9}SnI_3$ solar cells incorporating hot anti-solvent at 105 °C with/without FPEABr pre-annealing passivation. (a) J–V characteristics (the maximum PCE appended) and (b) EQE spectra (integrated J_{SC} appended) of the devices in the fully optimized architecture (5 mol% GeI_2,[2] ground Sn/SnF_2 additives,[28] vacuum treatments[2] and a PEDOT:PSS/PVK interlayer PEAI[2]). Solid and dotted lines correspond to forward and reverse J–V scans, respectively. (c) PL spectra (excitation at 400 nm, the peak wavelength appended) and (d) a SEM image of the 105 °C antisolvent with the FPEABr pre-annealing-passivated film (the scale bar: 1 μm).

in anti-solvent (EDA: ethylenediamine, Fig. S38 (SI)), and gas quenching (Fig. S39 (SI)). However, none of these approaches resulted in a simultaneous improvement in film morphology and PL intensity. Subsequently, we extensively screened twenty-two passivation agents (see Experimental) from the SEM/PL measurements (Note S3 (SI) and Fig. S40–S50 (SI)). The summary plot of SEM/PL (Fig. S51 (SI)) and device characterization (Fig. S52 (SI) and Tables S8–S9 (SI)) is provided in the SI. Note that passivation was applied during the spin-coating before the post-annealing, and thus, we term it pre-annealing treatment. Its comparison with the conventional passivation (passivation after post-annealing) is provided in the last part of this section. As a result, we identified 4-fluorophenethylammonium bromide (FPEABr) as the optimal passivator that enables well-packed morphology, increased PCE and resulted in good stability of Sn perovskites.

When integrated with our previously reported strategies (a use of a ground Sn–SnF_2 precursor,[28] PEAI interfacial modification of PEDOT:PSS[2] and vacuum treatments[2]), the PCE increases from 8.37% (6.65 ± 0.93%) for the 105 °C-only devices to 9.12% (7.99 ± 0.70%) upon FPEABr pre-annealing treatment (Fig. 5a and Table 1). The improvement primarily arises from an enhanced V_{OC} from 0.501 to 0.560 V, while J_{sc}, FF, and EQE (Fig. 5b) remain nearly unchanged. Accordingly, the structural and optoelectronic properties are also further improved (Fig. S53–S54 (SI)). In particular, the E_U decreases further from 36.7 meV to 33.5 meV by FPEABr passivation (Fig. S53c (SI)), along with the increase in XRD crystallite size (L_{100}) from 61.1 nm to 62.3 nm (Fig. S54a (SI)) and PL intensity (Fig. 5c). Notably, X-ray photoelectron spectroscopy (XPS) shows a significant reduction of Sn^{4+} in $Sn^{2+} + Sn^{4+}$ from 41.1% of the 65 °C-quenched film to 16.0% of the 105 °C-quenched film and further to 14.4% of the 105 °C-quenched film with FPEABr treatment (Fig. S55 (SI)). The SEM image (Fig. 5d) displays uniform and densely packed multi-grains, consistent with its improved V_{OC}. The photoabsorption and bandgap remain similar regardless of the FPEABr passivation, indicating minimal alternation of the fundamental photophysical properties of the perovskite absorber. These results indicate reduced band-tail states, improved lattice ordering, and effective defect passivation induced by thermally activated dimensional reconstruction on the grain surface.

Maximum power point tracking (MPPT) under 1 sun illumination with programmed dark interruptions demonstrates stable operation over time (Fig. S56 (SI) and Note S4 (SI)). The normalized PCEs slightly increase (1.02, 1.03, and 1.04), with no cumulative degradation after >14.5 h of total illumination. The fully reversible transient response indicates dynamic trap filling and ionic redistribution rather than irreversible degradation. The improved stability suggests defect passivation and favourable interfacial ionic rearrangement in the FPEABr-modified devices.

For a comparison, we examined the conventional post-annealing passivation (passivation after post thermal annealing) and FPEABr pre-annealing passivation for a 65 °C-quenched device in the same batch (Fig. S57–S58 (SI)), only using CB for pre-annealing dropping (Fig. S59 (SI)), along with

Table 1 Summary of $PEA_{0.1}FA_{0.9}SnI_3$ devices treated with 105 °C antisolvent only and treated with 105 °C antisolvent combined with FPEABr pre-annealing passivation[a]

Samples	PCE/%	V_{OC}/V	J_{SC}/mA cm^{-2}	FF	HI[b]	Sample count
105 °C	8.37 (6.65 ± 0.93)	0.501 (0.494 ± 0.013)	23.78 (22.61 ± 1.37)	0.703 (0.593 ± 0.053)	−0.050 (−0.058 ± 0.027)	20
105 °C w FPEABr	9.12 (7.99 ± 0.70)	0.560 (0.533 ± 0.029)	23.18 (22.83 ± 1.02)	0.703 (0.658 ± 0.049)	−0.098 (−0.103 ± 0.044)	57

[a] ITO/PEDOT:PSS/Sn perovskite/C_{60}/BCP/Ag. Values outside parentheses represent the maximum performance of the best device (taken from the forward scan), whereas the values in parentheses correspond to the average ± standard deviation. [b] Hysteresis index (HI) = (reverse PCE − forward PCE)/(reverse PCE).

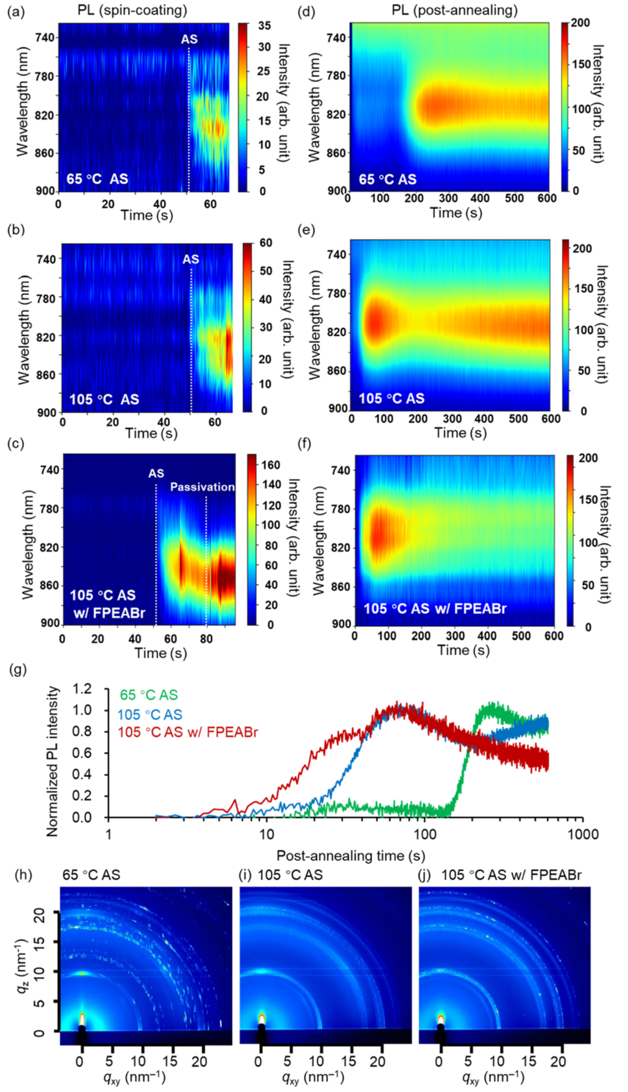

Fig. 6 *In situ* PL monitoring of $PEA_{0.1}FA_{0.9}SnI_3$ phase evolution during (a–c) spin-coating and (d–f) post-annealing and (g) extracted time-dependent PL intensity at 805 ± 5 nm during post-annealing. The time of AS and passivation is 53 and 79 s, respectively, and drawn with a dashed line. (h–j) Their 2D GIWAXS pattern profiles. (a), (d) and (h) 65 °C anti-solvent (AS) treatment, (b), (e) and (i) 105 °C AS treatment, and (c), (f) and (j) 105 °C AS treatment with FPEABr pre-annealing passivation.

FPEABr pre-annealing passivation for a 105 °C-quenched other formula (Fig. S60 (SI). As a result, our optimal condition (105 °C-quenching with FPEABr pre-annealing passivation) shows the highest PCE of 8.73% among the other conditions: 5.56% for 105 °C-quenching with FPEABr post-annealing passivation and 1.97% for 65 °C-quenching with FPEABr pre-annealing passivation (Fig. S57 (SI) and Table S10 (SI)). The results indicate that the introduction of FPEABr is effective when it is applied prior to the complete conversion to a multicrystalline film. Flat and densely packed grains observed in an SEM image of the 65 °C-quenched film with FPEABr passivation resemble those in the 105 °C-quenched film with FPEABr passivation (Fig. S58 (SI)). In contrast, the 105 °C-quenched film with FPEABr post-annealing shows distinct, multi grains with sharp boundaries, indicating that pre-annealing FPEABr passivation has a larger impact on the morphology than post-annealing passivation. The use of pure CB for pre-annealing passivation leads to significantly degraded film morphology and PL emission, suggesting that the observed improvements in performance and morphology arise from the passivator dissolved in CB (Fig. S59 (SI)). The 105 °C FPEABr passivation strategy also leads to enlarged grain size and enhanced PL emission compared to the other perovskite compositions ($FASnI_3$, Fig. S60 (SI)).

In situ PA and PL measurement for the FPEABr-passivated perovskite films

In situ PA and PL measurements were conducted to elucidate the crystallization dynamics during both spin coating and post-annealing processes. Although the PA profiles showed nearly identical evolution behaviour at different anti-solvent temperatures and under different FPEABr treatment conditions (Fig. S61–S62 (SI)), the PL evolution revealed substantial differences in nucleation and crystal growth pathways. During spin coating, the 65 °C AS film exhibited relatively weak PL intensity (Fig. 6a), indicating delayed nucleation, insufficient crystal nucleus formation, and prolonged existence of solvent-coordinated intermediate phases caused by inefficient DMSO extraction. In contrast, increasing the AS temperature to 105 °C significantly enhanced the PL intensity (Fig. 6b), suggesting accelerated DMSO removal, increased supersaturation, and formation of structurally ordered intermediate phases during the critical nucleation stage. Upon introducing FPEABr prior to annealing, the PL signal red-shifted and further intensified (Fig. 6c), implying interactions between the fluorinated organic cation and the perovskite framework, which likely induced local structural reconstruction and promoted more ordered intermediate-phase formation.

More distinct differences emerged during post-annealing. The 65 °C AS film showed a delayed PL rise beginning at ~140 s and gradual growth until ~250 s (Fig. 6d), indicating sluggish conversion from precursor intermediates to the emissive 3-dimensional (3D) perovskite. Such delayed crystallization leads to spatially nonuniform crystal growth and kinetically disordered nucleation. Furthermore, the slow crystallization suppresses efficient Ostwald ripening, where smaller grains dissolve and redeposit onto larger grains with lower surface energy, thereby limiting grain coarsening and crystal quality optimization. In contrast, the 105 °C AS films exhibited rapid PL rise during annealing and reached maximum intensity within ~70 s (Fig. 6e), while the FPEABr-treated film showed the earliest PL onset within ~30 s (Fig. 6f). The extracted 10–90% PL rise times (Fig. 6g) further confirmed accelerated formation of emissive 3D tin perovskites in the order of 65 °C AS < 105 °C AS < 105 °C AS w/FPEABr.

Correspondingly, grazing-incidence wide-angle X-ray scattering (GIWAXS) measurements of the 65 °C AS film (Fig. 6h and S63a (SI)) revealed weak 3D perovskite diffraction signals, indicating insufficient structural ordering and limited preferential orientation. The enhanced crystallization kinetics at 105 °

C facilitate thermodynamically stabilized crystal growth and more effective Ostwald ripening, resulting in improved grain growth and crystallinity. GIWAXS patterns of the 105 °C AS film (Fig. 6i and S63b (SI)) exhibited substantially enhanced diffraction peaks corresponding to the (100), (111), (200) and (210) planes, corresponding to the scattering vector (q) of 10, 17, 20, and 22 nm^{-1}. This indicates improved crystallinity and structural ordering. Despite no clear difference in I 3d XPS data with/without FPEABr (Fig. S64 (SI)), the enhanced GIWAXS peaks likely strengthened lattice binding and suppressed structural disorder, thereby prolonging the Ostwald ripening process and enabling further grain coarsening, defect healing, and lattice reconstruction. Consequently, the FPEABr-treated film exhibited the strongest and sharpest three-dimensional diffraction features (Fig. 6j and S63c (SI)). Upon completion of post-annealing, the 105 °C-quenched film with FPEABr pre-annealing passivation shows the highest PL intensity (Fig. 3d and 5c) along with a blue-shifted peak at *ca.* 880 nm. Since no 2D perovskite-originated PL peak and XRD peak were observed, FPEABr, a bulky 2D cation, is supposed to passivate the grain surface under the wet-conditions before the post-annealing process, which leads to an improvement in radiative recombination, V_{OC}, and PCE of the devices.

Collectively, this study establishes an effective crystallization-engineering strategy for advancing Sn-based perovskite photovoltaics through synergistic regulation of nucleation kinetics, intermediate-phase ordering and defect reconstruction. High-temperature anti-solvent quenching promotes rapid DMSO extraction and selects a temperature-governed intermediate-ordering pathway, which accelerates nucleation, facilitates thermodynamically stabilized crystal growth, suppresses energetic disorder, and broadens the processing window for reproducible film formation. Meanwhile, the subsequent pre-annealing FPEABr treatment further induces molecularly mediated lattice reconstruction and interfacial defect passivation through interactions between the fluorinated organic cation and the Sn–I framework. This process prolongs Ostwald ripening, enhances crystal orientation and grain coarsening, and suppresses band-tail states and non-radiative recombination. As a result, the synergistic combination of thermally accelerated crystallization and fluorinated molecular passivation provides a coherent mechanistic framework for simultaneously enhancing the efficiency, operational stability, and reproducibility (Fig. S65 (SI)) of Sn-based perovskite solar cells.

Although the champion PCE of 9.12% remains below that of the current state-of-the-art Sn-based perovskite solar cells exceeding 17.71%,[62] this work highlights the critical importance of regulating intermediate-phase evolution, defect formation, and crystal growth kinetics in PEA-containing Sn perovskites. Distinct from the majority of recent strategies summarized in Table S11 (SI) that primarily focus on modifications prior to or after film formation, our work specifically targets the regulation of the crystallization process itself. The proposed high-temperature anti-solvent quenching and pre-annealing passivation strategy provides mechanistic insights into controlling crystallization dynamics, wet-film interfacial reconstruction, and non-radiative recombination in Sn-based perovskites. Nevertheless, the device efficiency is still limited by residual defect-assisted non-radiative recombination, Sn^{2+} oxidation, energetic disorder, defect-rich grain boundaries, non-optimized interfacial charge transport, and limited operational stability. The results of this work suggest that the simultaneous regulation of crystallization behaviour and interfacial defect reconstruction represents a promising direction for the development of highly efficient and stable Sn-based perovskite solar cells. Furthermore, future studies combining the present thermal engineering strategy with advanced defect passivation, interface engineering, oxidation suppression, and scalable fabrication approaches may further improve the PCE and operational stability of Sn-based PSCs.

Conclusions

We demonstrate that the crystallization process of Sn-based perovskites can be addressed by temperature control of anti-solvent. The hot anti-solvent treatment (HAT at 105 °C) generates a structurally ordered intermediate phase at the critical nucleation moment, leading to enhanced photophysical characteristics (increased PL and reduced E_U) and improved SEM-observed multi-grains (dense packing without pin holes). Importantly, this optimal HAT method largely decouples the effects of other process parameters such as anti-solvent timing, height and post-thermal annealing, which improves the PCE, stability and reproducibility of Sn-based PSCs. Beyond nucleation control, pre-annealing FPEABr passivation reprograms the annealing stage and effectively decreases defects. As a result, HAT at 105 °C with pre-annealing FPEABr passivation improved the PCE from 3.50% to 9.12%, owing to the increase in V_{OC} associated with the reduced non-radiative recombination. Our findings establish a mechanistic framework, in which nucleation stabilization and pre-thermal passivation act sequentially yet synergistically, paving a way to reproducible, stable, and high-efficiency lead-free Sn PSCs.

Experimental

Materials

Deoxidized dimethyl sulfoxide (DMSO), deoxidized *N*,*N*-dimethylformamide (DMF), deoxidized toluene, chlorobenzene (CB) and L-phenylalanine hydrochloride (L-PhAHCl) were purchased from Wako-Fuji Film Industries Ltd and used as received. Methylammonium thiocyanate (MASCN), *n*-octylammonium bromide (OABr), 4-fluorophenethylammonium iodide (FPEAI), formamidinium iodide (FAI), phenethylammonium iodide (PEAI), and phenethylammonium chloride (PEACl) were purchased from GreatCell Solar (Australia). Phenethylammonium bromide (PEABr) was purchased from Xi'an Yuri Solar Co., Ltd (China). Methylammonium chloride (MACl), methylammonium iodide (MAI), methylammonium bromide (MABr), glycine hydrochloride (GlyHCl), 2-(4-fluorophenyl)ethylamine hydrochloride (FPEACl), diethylammonium iodide (DEAI), imidazole hydroiodide (ImHI), dimethylamine hydroiodide (DMAI), (2,2′-(1,2-

phenylene)bis(ethan-1-amine) dihydroiodide ($PDEAI_2$), 1,3-diaminopropane dihydroiodide ($PDAI_2$), 4-fluorophenethylammonium bromide (FPEABr), oxamic acid potassium salts (OAPs), C_{60} and bathocuproine (BCP, purified by sublimation, 99.0%) were purchased from Tokyo Chemical Industry Co. Ltd. SnF_2 (99%) and Sn powder (99.8% trace metals) were purchased from Wako-Fuji Film Industries Ltd. Ethylene diammonium diiodide ($EDAI_2$), ammonium thiocyanate (NH_4SCN), SnI_2 (anhydrous, beads, 99.99% trace metals basis) and germanium(II) iodide (GeI_2) were purchased from Sigma-Aldrich. They were used without further purification.

Precursor preparation

A 0.8 M DMSO solution of $PEA_{0.1}FA_{0.9}SnI_3$ with ground Sn–SnF_2 powder[28] and Sn powder was applied in the whole study. For example, 19.9 mg PEAI, 123.8 mg FAI, 298.0 mg SnI_2, 25 mg ground Sn–SnF_2 powder,[28] 237.5 mg Sn powder, and 13.1 mg GeI_2 (ref. 2) were weighed and dissolved in 1 mL DMSO and rigorously stirred at 45 °C for longer than 2 h in an N_2-filled glove box (O_2 < 1 ppm, H_2O < 1 ppm).

Preparation of pre-annealing passivator solution

A saturated concentration (<1 mg mL^{-1}) of 22 passivation agents ($EDAI_2$, MACl, MAI, MABr, MASCN, PEAI, PEACl, PEABr, GlyHCl, L-PhAHCl, FPFACl, DEAI, ImHI, DMAI, $PDEAI_2$, $PDAI_2$, NH_4SCN, CsSCN, OABr, FPEABr, FPEAI, and OAPs) were dissolved in CB. The precursor solutions were stirred overnight at room temperature. And then, the solutions after 0.22 μm filtering were dynamically spin-coated on the ITO/PEDOT:PSS/PEAI/Sn perovskite at 4000 rpm for 20 s. A transparent brownish film was thermally annealed on a hot plate at 45, 65, and 100 °C for 10 min each, which led to a gradual change in colour to deeper.

Device fabrication and characterization

Under ambient conditions, a PEDOT:PSS layer (Clevios P VP AI 4083) was deposited on cleaned ITO (155 nm in thickness, 2.5 × 2.5 cm^2 in size, ~90% transmittance at 550 nm, <10 Ω sq^{-1}) on a glass by spin-coating at a slope of 5 s, 5000 rpm for 60 s, and slope of 1 s followed by thermal annealing at 140 °C for 20 min. A vacuum treatment and an interlayer PEAI between the PEDOT:PSS layer and perovskite layer were applied as in our reported paper.[2] In an N_2-filled glovebox, the precursor solution just after filtering Sn powder off was dropped on ITO/PEDOT:PSS/PEAI and spun at a slope of 5 s, 5000 rpm for 60 s, and slope of 1 s. At the total collapse time of 53 s, 360 μL toluene at designated temperatures (13–135 °C) was continuously dropped within 1 s by using an φ ~2 mm dry pipette tip (1 mL size) at an appropriate position. In the case of pre-annealing passivation, after 10 s of interval spin-coating was resumed with a 3 s slope and 4000 rpm for 20 s. A CB solution containing the passivator was dropped at 79 s from the start of the process, calculated as the sum of 5 s for ramping, 60 s for static spin-coating of the perovskite precursor, 1 s for ramping, 10 s for passivator solution preparation, 3 s for ramping, and 20 s for dynamic spin-coating. A transparent brownish film was thermally annealed on a hot plate at 45, 65, and 100 °C for 10 min each (three steps) or 80 °C for 20 min (one step), which led to a gradual change in colour to deeper. The films were transferred to a vacuum chamber (<10^{-4} Pa) and kept for 2 h (vacuum treatment of Sn perovskite),[2] and a 20 nm-thick C_{60} layer was thermally deposited at ~0.1 Å s^{-1} (<10 nm) and ~0.2 Å s^{-1} (>10 nm). After being replaced by a nine-dot blank mask, 8 nm-thick BCP at ~0.1 Å s^{-1} and 100 nm-thick Ag layers at ~0.1 Å s^{-1} (<10 nm), ~0.2 Å s^{-1} (10 nm~ 20 nm) and ~0.5 Å s^{-1} (>20 nm) were sequentially deposited in a vacuum chamber. Current density–voltage curves were measured using a source meter unit (SMU) (ADCMT Corp., 6241A or Keysight B2910BL) under AM1.5 G pseudo-solar illumination at 100 mW cm^{-2} using a 300 W Xe-lamp solar simulator (SAN-EI Corp., XES-30, class A) or an LED solar simulator (LumiSun-50, Innovation in Optics Inc. USA, IEC class A^+A^+A). The output powers of the solar simulators were monitored using a calibrated silicon standard cell of Bunko Keiki BS-501BK with a Sigma-Koki Inc. HAF-50H heat absorbing short-pass filter. The output of the standard cell with the filter was calibrated by EQE measurements. The device was packed in a measurement chamber with a light mask (area = 0.0314 cm^2; the area of the device = 0.071 cm^2). The scan was conducted from −0.1 to 0.7 V and then backwards, with a step size of 0.02 V, a hold time of 150 ms, a compliance current of 20 mA, an integration time of 10 ms, and a measurement delay of 100 ms. The EQE spectra were recorded using a Bunko Keiki SM-250KD equipped with a Keithley 2401 SMU. The monochromatic light power of the EQE instrument was calibrated using a silicon photovoltaic cell (Bunko Keiki model S1337-1010BQ). All the measurements were performed at 25 °C in the air.

General measurement

Steady-state photoabsorption and photoluminescence spectroscopies were performed using a Jasco V-730 ultraviolet-visible (UV-vis) and Jasco FP-8300 spectrophotometers, respectively. XRD measurements were performed using a Rigaku Corp. MiniFlex-600 instrument (Cu Kα radiation $\lambda = 1.54$ Å). XPS measurements were performed on a Shimadzu KRATOS ULTRA2, and the data were analysed using KherveFitting software. SEM measurements were performed on a JEOL JSM-IT700HR (5 keV, 50 μA), and the grain size was evaluated using the MorphoLibJ library in ImageJ software. 2D-GIWAXS experiments were performed on the beam line BL13XU or BL16XU at SPring-8 (12.39 keV, $\lambda = 1$ Å X-ray). The 2D-GIWAXS patterns were monitored with a 2D image detector (Pilatus 300 K).

In situ optical spectroscopy

In situ UV-vis absorption and PL spectroscopy were performed using a StellarNet spectrometer (UV-vis: BLACK-Comet; PL: SILVER-Nova), a Xe lamp (for UV-vis, Hamamatsu Photonics, C12122-020-57-C2), and a UV-LED (for PL excitation, ASAHI Spectra, CL-H1-470-9-1-B 470 nm). The measurements were performed inside a N_2-filled glove box.[51] The details were reported previously.

Author contributions

T. L. designed the research and performed all the experiments. R. N. supported *in situ* PA/PL measurements and their analysis. C.-Y. C. and A. W. advised and suggested the improvement in Sn-PSC fabrication and characterization. A. S. led the project, funding acquisition, and supervision. T. L. prepared the initial draft and figure items, and A. S. thoroughly edited and revised them. All the authors discussed the results, read the manuscript and gave feedback.

Conflicts of interest

The authors declare no competing financial interests.

Data availability

The dataset is available in the supplementary information (SI). Supplementary information: anti-solvent temperature screening and 1-step *vs.* 3-step annealing (Fig. S1–S13, Tables S1–S3, and Note S1); five-parameter process tolerance (Fig. S14–S31, Tables S4–S7 and Note S2); further explored numerous strategies (Fig. S32–S39); pre-annealing passivation (Fig. S40–S60, Tables S8–S10, and Notes S3–S5); time-resolved *in situ* PA monitoring (Fig. S61–S62); 1D line-cut profiles from 2D GIWAXS patterns (Fig. S63); comparative XPS analysis of iodine chemical states (Fig. S64) (PDF). See DOI: https://doi.org/10.1039/d6ta03298b.

Acknowledgements

We acknowledge the financial support received from the Japan Science and Technology Agency (JST) CREST (JPMJCR23O2 to A. S.) and MIRAI (JPMJMI22E2 to A. W. and A. S.), the New Energy and Industrial Technology Development Organization (NEDO) Green Innovation Project (JP21578854 to A. W. and A. S.), and KAKENHI of the Japan Society for the Promotion of Science (JSPS) (JP20H05836 and JP24H00484 to A. S. and JP23K13826 and JP25K01857 to R. N.). We are grateful to Dr Tomoyuki Koganezawa at JASRI for his support with the 2D-GIXRD experiments, which were conducted at SPring-8, JASRI, with proposal numbers of 2025B1987 and 2026A1033. This research was partially supported by Research Support Project for Life Science and Drug Discovery (Basis for Supporting Innovative Drug Discovery and Life Science Research (BINDS)) from AMED under Grant Number JP24AMA121054. We gratefully acknowledge Mr R. Shimomura at The University of Osaka for his assistance with the operation of the *in situ* monitoring system.

References

1 A. Shukla, D. B. Khadka, C. Li, M. Rikukawa, Y. Takeoka, R. Sahara, M. Yanagida and Y. Shirai, *J. Mater. Chem. A*, 2025, **13**, 23487–23498.
2 T. Liu, R. Nishikubo, A. Wakamiya and A. Saeki, *ACS Appl. Energy Mater.*, 2026, **9**, 2229–2238.
3 V. Stacchini, M. Rastgoo, M. Marčinskas, C. Frasca, K. Morita, L. Frohloff, A. Treglia, T. W. Gries, O. Karalis, V. Getautis, F. Ruske, A. Petrozza, N. Koch, H. Hempel, T. Malinauskas, A. Abate and A. Musiienko, *Adv. Energy Mater.*, 2025, **15**, 2500841.
4 Y. Ma, J. Wu, Z. Wu, M. H. Mahyuddin and Z. Liang, *Adv. Funct. Mater.*, 2026, **36**, e12300.
5 F. Iyoda, R. Nishikubo, A. Wakamiya and A. Saeki, *ACS Appl. Energy Mater.*, 2020, **3**, 8224–8232.
6 C. Nishikawa, R. Nishikubo, F. Ishiwari and A. Saeki, *ACS Appl. Energy Mater.*, 2022, **5**, 6291–6301.
7 C. Nishikawa, R. Nishikubo, F. Ishiwari and A. Saeki, *JACS Au*, 2023, **3**, 3194–3203.
8 M. Sun, Z. Zhao, H. Xu, Y. Li, J. Gao, F. Xiang, H. Meng, Y. Chen, T. Liu, X. Wu, Z. Fink, Y. Li, H. Ding, J. Zhu, D. Luo, Z. Xiao, T. P. Russell and Q. Hu, *Nano Lett.*, 2025, **25**, 3103–3112.
9 L. Chen, L. Di Mario, G. Portale, C. J. Brabec and M. A. Loi, *Adv. Energy Mater.*, 2026, **16**, e03611.
10 R. Nishikubo, N. Ishida, Y. Katsuki, A. Wakamiya and A. Saeki, *J. Phys. Chem. C*, 2017, **121**, 19650–19656.
11 E. Nakanishi, R. Nishikubo, F. Ishiwari, T. Nakamura, A. Wakamiya and A. Saeki, *ACS Mater. Lett.*, 2022, **4**, 1124–1131.
12 S. Li, Y. Jiang, J. Xu, D. Wang, Z. Ding, T. Zhu, B. Chen, Y. Yang, M. Wei, R. Guo, Y. Hou, Y. Chen, C. Sun, K. Wei, S. M. H. Qaid, H. Lu, H. Tan, D. Di, J. Chen, M. Grätzel, E. H. Sargent and M. Yuan, *Nature*, 2024, **635**, 82–88.
13 Z. Liang, Y. Zhang, H. Xu, W. Chen, B. Liu, J. Zhang, H. Zhang, Z. Wang, D.-H. Kang, J. Zeng, X. Gao, Q. Wang, H. Hu, H. Zhou, X. Cai, P. Reiss, B. Xu, T. Kirchartz, Z. Xiao, S. Dai, N.-G. Park, J. Ye and X. Pan, *Nature*, 2023, **624**, 557–563.
14 H. Gao, K. Xiao, R. Lin, S. Zhao, W. Wang, S. Dayneko, C. Duan, C. Ji, H. Sun, A. D. Bui, C. Liu, J. Wen, W. Kong, H. Luo, X. Zheng, Z. Liu, H. Nguyen, J. Xie, L. Li, M. I. Saidaminov and H. Tan, *Science*, 2024, **383**, 855–859.
15 Y. Zheng, Y. Li, R. Zhuang, X. Wu, C. Tian, A. Sun, C. Chen, Y. Guo, Y. Hua, K. Meng, K. Wu and C.-C. Chen, *Energy Environ. Sci.*, 2024, **17**, 1153–1162.
16 W. Shockley and H. J. Queisser, *J. Appl. Phys.*, 1961, **32**, 510–519.
17 C. C. Stoumpos, C. D. Malliakas and M. G. Kanatzidis, *Inorg. Chem.*, 2013, **52**, 9019–9038.
18 J. Chen, J. Luo, E. Hou, P. Song, Y. Li, C. Sun, W. Feng, S. Cheng, H. Zhang, L. Xie, C. Tian and Z. Wei, *Nat. Photonics*, 2024, **18**, 464–470.
19 P. F. Chan, M. Qin, C.-J. Su, L. Ye, X. Wang, Y. Wang, X. Guan, Z. Lu, G. Li, T. Ngai, S. W. Tsang, N. Zhao and X. Lu, *Adv. Sci.*, 2024, **11**, 2309668.
20 J. Choi, S. J. Yang, S. G. Han, W. Sung, D. Yoo and K. Cho, *Chem. Mater.*, 2023, **35**, 1148–1158.
21 L. Wang, Q. Miao, D. Wang, M. Chen, H. Bi, J. Liu, A. K. Baranwal, G. Kapil, Y. Sanehira, T. Kitamura, T. Ma, Z. Zhang, Q. Shen and S. Hayase, *Angew. Chem., Int. Ed.*, 2023, **62**, e202307228.

22 L. Wang, M. Chen, S. Yang, N. Uezono, Q. Miao, G. Kapil, A. K. Baranwal, Y. Sanehira, D. Wang, D. Liu, T. Ma, K. Ozawa, T. Sakurai, Z. Zhang, Q. Shen and S. Hayase, *ACS Energy Lett.*, 2022, **7**, 3703–3708.

23 F. Yang, K. Wang, Y. Yang, Y. Chen, Z. Kang, T. Li, R. Sun, Y. Tong and H. Wang, *Nano Lett.*, 2025, **25**, 5957–5964.

24 Y. Zhang, S. Ge, C. Pu, J. Xu, Y. Xiao, X. Wang, W. Zhai, Z. Yan, H. Xie, P. Teng, T. Yu, J. Yang and C. Bao, *Nano Lett.*, 2025, **25**, 13095–13102.

25 J. Wang, Z. Gao, J. Yang, M. Lv, H. Chen, D.-J. Xue, X. Meng and S. Yang, *Adv. Energy Mater.*, 2021, **11**, 2102131.

26 Z. Zhang, Y. Huang, J. Jin, Y. Jiang, Y. Xu, J. Zhu and D. Zhao, *Angew. Chem., Int. Ed.*, 2023, **62**, e202308093.

27 D. He, P. Chen, H. Xu, F. Kremer, M. Zhang, J. A. Steele, Z. Wang, S. Ding, C. Zhang, T. Lin, H. Xu, M. Hao and L. Wang, *Nat. Nanotechnol.*, 2025, **20**, 779–786.

28 T. Liu, S. Cho, R. Nishikubo, M. Pylnev, F. Ishiwari, A. Wakamiya and A. Saeki, *EES Sol.*, 2025, **1**, 78–88.

29 J. Zillner, H.-G. Boyen, P. Schulz, J. Hanisch, N. Gauquelin, J. Verbeeck, J. Küffner, D. Desta, L. Eisele and E. Ahlswede, *Adv. Funct. Mater.*, 2022, **32**, 2109649.

30 X. Wan, C. Xu, H. Wang, Z. Jiang, F. Li, G. Xu, Z. Dai, X. He and Q. Song, *Small*, 2024, **20**, 2401136.

31 J. Pascual, M. Flatken, R. Félix, G. Li, S.-H. Turren-Cruz, M. H. Aldamasy, C. Hartmann, M. Li, D. Di Girolamo, G. Nasti, E. Husam, R. G. Wilks, A. Dallmann, M. Bär, A. Hoell and A. Abate, *Angew. Chem., Int. Ed.*, 2021, **60**, 21583–21591.

32 D. Meggiolaro, L. Gregori and F. De Angelis, *ACS Energy Lett.*, 2023, **8**, 2373–2375.

33 F. Gu, S. Ye, Z. Zhao, H. Rao, Z. Liu, Z. Bian and C. Huang, *Sol. RRL*, 2018, **2**, 1800136.

34 E. Nakanishi, R. Nishikubo, A. Wakamiya and A. Saeki, *J. Phys. Chem. Lett.*, 2020, **11**, 4043–4051.

35 J. Liu, M. Ozaki, S. Yakumaru, T. Handa, R. Nishikubo, Y. Kanemitsu, A. Saeki, Y. Murata, R. Murdey and A. Wakamiya, *Angew. Chem., Int. Ed.*, 2018, **57**, 13221–13225.

36 K. Nishimura, M. A. Kamarudin, D. Hirotani, K. Hamada, Q. Shen, S. Iikubo, T. Minemoto, K. Yoshino and S. Hayase, *Nano Energy*, 2020, **74**, 104858.

37 M. Chen, M.-G. Ju, H. F. Garces, A. D. Carl, L. K. Ono, Z. Hawash, Y. Zhang, T. Shen, Y. Qi, R. L. Grimm, D. Pacifici, X. C. Zeng, Y. Zhou and N. P. Padture, *Nat. Commun.*, 2019, **10**, 16.

38 T. Nakamura, S. Yakumaru, M.-A. Truong, K. Kim, J. Liu, S. Hu, K. Otsuka, R. Hashimoto, R. Murdey, T. Sasamori, H.-D. Kim, H. Ohkita, T. Handa, Y. Kanemitsu and A. Wakamiya, *Nat. Commun.*, 2020, **11**, 3008.

39 X. Meng, Y. Wang, J. Lin, X. Liu, X. He, J. Barbaud, T. Wu, T. Noda, X. Yang and L. Han, *Joule*, 2020, **4**, 902–912.

40 M. H. Kumar, S. Dharani, W. L. Leong, P. P. Boix, R. R. Prabhakar, T. Baikie, C. Shi, H. Ding, R. Ramesh, M. Asta, M. Grätzel, S. G. Mhaisalkar and N. Mathews, *Adv. Mater.*, 2014, **26**, 7122–7127.

41 J.-W. Lee, S. Tan, T.-H. Han, R. Wang, C. Choi, M. Yoon, C. Zhu, K. Huynh, M. S. Goorsky, Y. Huang, L. Zhang, C. Park, M. Xu, M. E. Liao, S.-J. Lee, X. Pan, S. Nuryyeva and Y. Yang, *Nat. Commun.*, 2020, **11**, 5514.

42 H. Li, X. Jiang, Q. Wei, Z. Zang, M. Ma, F. Wang, W. Zhou and Z. Ning, *Angew. Chem., Int. Ed.*, 2021, **60**, 16330–16336.

43 Y. Liao, H. Liu, W. Zhou, D. Yang, Y. Shang, Z. Shi, B. Li, X. Jiang, L. Zhang, L. N. Quan, R. Quintero-Bermudez, B. R. Sutherland, Q. Mi and Z. Ning, *J. Am. Chem. Soc.*, 2017, **139**, 6693–6699.

44 M. A. Flatken, E. Radicchi, R. Wendt, A. G. Buzanich, E. Härk, J. Pascual, F. Mathies, O. Shargaieva, A. Prause, A. Dallmann, F. De Angelis and A. Hoell, *Chem. Mater.*, 2022, **34**, 1121–1131.

45 R. Quintero-Bermudez, A. Gold-Parker, Z. Yang, S. O. Kelley, A. H. Proppe, R. Munir, A. Amassian, M. F. Toney and E. H. Sargent, *Nat. Mater.*, 2018, **17**, 900–907.

46 J. Zhang, J. Qin, M. Wang, Y. Bai, H. Zou, J. K. Keum, R. Tao, H. Xu, H. Yu, S. Haacke and B. Hu, *Joule*, 2019, **3**, 3061–3071.

47 X. Zhang, X. Ren, B. Liu, R. Munir, J. Li, Y. Liu, D.-M. Smilgies, X. Zhu, D. Yang, R. Li, Z. Yang, T. Niu, X. Wang, A. Amassian, K. Zhao and S. Liu, *Energy Environ. Sci.*, 2017, **10**, 2095–2102.

48 Z. Guo, Y. Zhang, B. Wang, L. Wang, N. Zhou, Z. Qiu, N. Li, Y. Chen, C. Zhu, H. Xie, T. Song, L. Song, H. Xue, S. Tao, Q. Chen, G. Xing, L. Xiao, Z. Liu and H. Zhou, *Adv. Mater.*, 2021, **33**, 2102246.

49 J. Wang, G. Chen, S. Luo, Y. Lin, T. Huang, S. Xiao, Y. Chen, H. Huang, Y. Deng, Z. Li, C. Zhou, L. Ding, K. Meng, J. He, J. Huang and Y. Yuan, *Nat. Commun.*, 2020, **11**, 582.

50 S. Sidhik, I. Metcalf, W. Li, T. Kodalle, C. J. Dolan, M. Khalili, J. Hou, F. Mandani, A. Torma, H. Zhang, R. Garai, J. Persaud, A. Marciel, I. A. Muro Puente, G. N. M. Reddy, A. Balvanz, M. A. Alam, C. Katan, E. Tsai, D. Ginger, D. P. Fenning, M. G. Kanatzidis, C. M. Sutter-Fella, J. Even and A. D. Mohite, *Science*, 2024, **384**, 1227–1235.

51 Q. He, Y. Bao, S. Pan, T. Zhang, X. Wang, Y. Yang, Q. Guo, J. Qiao, J. Li and J. Pan, *J. Mater. Chem. A*, 2026, **14**, 14292–14299.

52 L. Qin, M. Zhu, Y. Xia, X. Ma, D. Hong, Y. Tian, Z. Tie and Z. Jin, *Nano Res.*, 2024, **17**, 5131–5137.

53 L. Jiang, L. Yao, F. Zhou, Z. Wen, H. Zhang, H. Zheng, M. Ye, Z. Gao, Y. Zheng, X. Luo, D. Wang and X. Liu, *J. Mater. Chem. A*, 2026, **14**, 18021–18030.

54 L. Qin, M. Zhu, M. Zhang, J. Liang, X. Ma, P. Zhang, D. Hong, Y. Wang, Y. Tian, H. Sun, Z. Tie, Y. Xiong and Z. Jin, *Nano Lett.*, 2025, **25**, 7053–7060.

55 M. Zhu, Y. Xia, L. Qin, K. Zhang, J. Liang, C. Zhao, D. Hong, M. Jiang, X. Song, J. Wei, P. Zhang, Y. Tian and Z. Jin, *Nano Res.*, 2023, **16**, 6849–6858.

56 J. Huang, X. Li, Z. Zhang, T. Sun, H. Dong, H. Yu, X. Ma, W. Yang, L. Dai, L. Wang, B. Hu, Y. Shen, M. K. Nazeeruddin and M. Wang, *Adv. Mater.*, 2026, **38**, e11684.

57 Y. Gao, Y. Li, G. Liu, N. Zhang, S. Li, Z. Wang, Z. Lv, Y. Zhang, L. Yang, J. Zhang, L. Zhang, W. Li, W. Tian, W. Li, Z. Ying, J. Qiu and Y. Shi, *Energy Environ. Sci.*, 2026, **19**, 691–701.

58 S. Wang, W. Tian, Z. Cheng, X. Shi, W. Fan, J. Zhou, D. Gu, J. Xue and R. Wang, *Nat. Energy*, 2025, **10**, 1074–1083.

59 K. Dong, L. Zhu, G. Yang, L. Zheng, Y. Wang, B. Zhang, J. Zhou, J. Bian, F. Zhang, S. Yu, S. Liu, M. Wang, J.-D. Xiao, X. Guo and X. Jiang, *ChemSusChem*, 2024, **17**, e202400038.

60 Y. Xia, M. Zhu, L. Qin, C. Zhao, D. Hong, Y. Tian, W. Yan and Z. Jin, *Energy Mater.*, 2023, **3**, 300004.

61 Y. Park, R. Nishikubo, M. Pylnev, R. Shimomura and A. Saeki, *ACS Appl. Energy Mater.*, 2024, **7**, 11818–11826.

62 T. Li, X. Luo, P. Wang, Z. Li, Y. Li, J. Huang, Z. Jin, Y. Yang, B. Li, W. Zhang, S. Lin, Y. Rui, H. Wang, Q. Zhang, Y. Zhan, B. Xu, J. Liang and Y. Qi, *Nature*, 2025, **648**, 84–90.